Rivet analysis of K^0_S- and (anti-) Λ-hadron correlations in pp collisions at $\sqrt{s} = 13\,\mathrm{TeV}$

Bachelor Thesis

Daniel Günther
Matr.-Nr. 432141

Westfälische Wilhelms-Universität Münster
Institut für Kernphysik
AG Andronic / Klein-Bösing

Referees:
Prof. Dr. Anton Andronic
Prof. Dr. Christian Klein-Bösing

Münster, September 20, 2021

Declaration of Academic Integrity

I, *Daniel Günther*, hereby confirm that this thesis on "RIVET analysis of K^0_S- and (anti-) Λ-hadron correlations in pp collisions at $\sqrt{s} = 13\,\text{TeV}$" is solely my own work and that I have used no sources or aids other than the ones stated. All passages in my thesis for which other sources, including electronic media, have been used, be it direct quotes or content references, have been acknowledged as such and the sources cited.

Place, Date

Daniel Günther

I agree to have my thesis checked in order to rule out potential similarities with other works and to have my thesis stored in a database for this purpose.

Place, Date

Daniel Günther

Nature has alway looked like a horrible mess, but as we go along we see patterns and put theories together; a certain clarity comes and things get simpler.

Richard P. Feynman

Contents

1 Introduction **5**

2 Theory **7**

2.1 Standard model of particle physics 7

2.2 K^0_S meson and (anti-) Λ hyperon 8

2.3 Kinematics in detector physics 9

3 Methods **11**

3.1 Large Hadron Collider 11

3.2 ALICE 12

3.3 PYTHIA 14

3.4 RIVET 16

3.4.1 Overview 16

3.4.2 Structure and usage 16

4 Analysis **20**

4.1 Multiplicity Selection 20

4.2 Correlations 20

4.3 Transverse Momentum Selection 21

4.4 Per Trigger Normalization 21

4.5 Correction - Mixed Event Method 22

4.6 Projection on azimuthal angle 22

4.7 Peak Yields 23

4.8 Uncertainties 23

5 Results and Discussion **25**

5.1 Per-trigger Yields 25

5.2 Comparison with experimental data 27

5.3 Comparison of Hadron- and Strangeness-Triggered Yields 28

6 Conclusion and Outlook **32**

List of Figures **33**

References **33**

Appendix **35**

1 Introduction

Based on data of proton-proton collisions taken with the ALICE experiment at the Large Hadron Collider, particle production as a function of event-activity and particle transverse momentum is studied to deepen understanding of physical processes involved in hadronization. "[D]ifferences between quark- and gluon-initiated jets in e^+-e^- annihilations have been revealed in several measurements. Gluon jets are characterised by larger charged-particle multiplicity than quark jets. Moreover, in the relative production of K^0_S mesons and Λ hyperons to charged particles, it was found that the relative production of Λ is $\approx 30\%$ higher in gluon than in quark jets, while the relative K^0_S production was found to be approximately the same." [Col21]

Continuing research in this regard, effects of a strangeness bias, "both in form of a meson (K^0_S) and baryon (Λ)" [Col21], are studied with the dihadron correlation approach, whereas a charged-hadron, K^0_S meson or $(\overline{\Lambda})\Lambda$ hyperon with a transverse momentum within $3\,\mathrm{GeV} < p_T^{trigger} < 20\,\mathrm{GeV}$ is used as a trigger particle and a charged-hadron within $1\,\mathrm{GeV} < p_T^{assoc} < p_T^{trigger}$ as associated particle. Like this, two-particle correlations are constructed from proton-proton collisions with a collision energy of $\sqrt{s} = 13\,\mathrm{TeV}$ for different event-activity classes and trigger (associated) particle momentum intervals as functions of azimuthal angle and pseudorapidity. "Such correlations encode effects of fragmentation, hadronisation and parton showering as well as possible collectivity and jet quenching."[Col21] To evaluate effects of multiplicity, particle momentum and the strangeness bias per-trigger particle yields for the azimuthal near- and away-side are extracted from the correlation functions and again interpreted as functions of multiplicity and particle momentum. This reveals a reduction in charged-hadron production with occurrence of a K^0_S meson in all multiplicity classes, constant for different particle momenta, and a multiplicity and particle momentum dependent change with the occurrence of a $(\overline{\Lambda})\Lambda$ hyperon. Exploring the machinations associated with this observations, results of such studies are compared to model predictions with different involved processes either in- or excluded. Therefore, collision events are simulated with Monte Carlo generators such as PYTHIA. As comparison of experimental data and model prediction is key, an independent tool to analyse modelled events and relate them to data is of great value.

The established method is to implement such an analysis in the RIVET framework, which was done for this thesis. On the following pages the theoretical and experimental background is given and the technical approach on the analysis is described. Eventually, only minor physical conclusions are drawn from the analysis to to the fact that it was only

run on a sample of 8 million events yet, which doesn't produce statistically significant results. Nonetheless, the run provides a basis to discuss and demonstrate functionality.

2 Theory

2.1 Standard model of particle physics

In modern physics the subnuclear level of matter and interactions is described with the Standard Model of Particle Physics (SM). The SM postulates the existence of three forces in particle interactions - the electromagnetic force, the weak force and the strong force - and three kinds of elementary particles - quarks and leptons, which are called fermions, and bosons, the messenger particles in the quantum field theory of their corresponding force. As of today, gravitation is not included in the SM because the graviton, the boson carrying gravitation, was not experimentally proven yet. Furthermore, gravitation can be neglected on this scale due to its relative weakness.

The matter particles quarks and leptons are further organized into three generations with four elementary particles each. The first generation of particles consists of the up and down quark, as well as the electron and electron-neutrino which can be distinguished by their interactions. The up and down quarks carry an electric charge of $\frac{2}{3}$ and $-\frac{1}{3}$ determining their electromagnetic interactions, a color charge of red, green or blue corresponding to the strong force and a weak charge for the weak force. The corresponding particles in second and third generation only differ in mass from the first generation, forming the first three columns of Fig. 1. Moreover, for each particle there is an anti-particle which makes up anti-matter.

The electromagnetic force between charged particles is transmitted by electrically uncharged, colorless photons and is described by quantum electrodynamics (QED). The strong force is mediated by neutral, colored gluons and is described by quantum chromodynamics (QCD). In contrast to quarks, which carry any given color or anti-color, the gluon's color charge consists of any color - anti-color combination. Z^0- and $W^{\pm}$-bosons are the messenger particles of the weak force, described by quantum flavourdynamics (QFD), which less significant to this work as the former two. Two bound quarks have a potential energy of: [Pov+14]

$$E_{pot} = -\frac{A}{r} + Br \tag{1}$$

Equation 1 describes a superposition of the electrostatic force, increasing with $-\frac{1}{r}$, and the strong force, increasing with r. It was experimentally observed that quarks can not be found individually, but only in composite color-neutral particles called hadrons. This is called *confinement* and inspired the linear component in equation 1. By separating bound quarks from one another, as it happens in high energy proton-proton (pp) collisions for

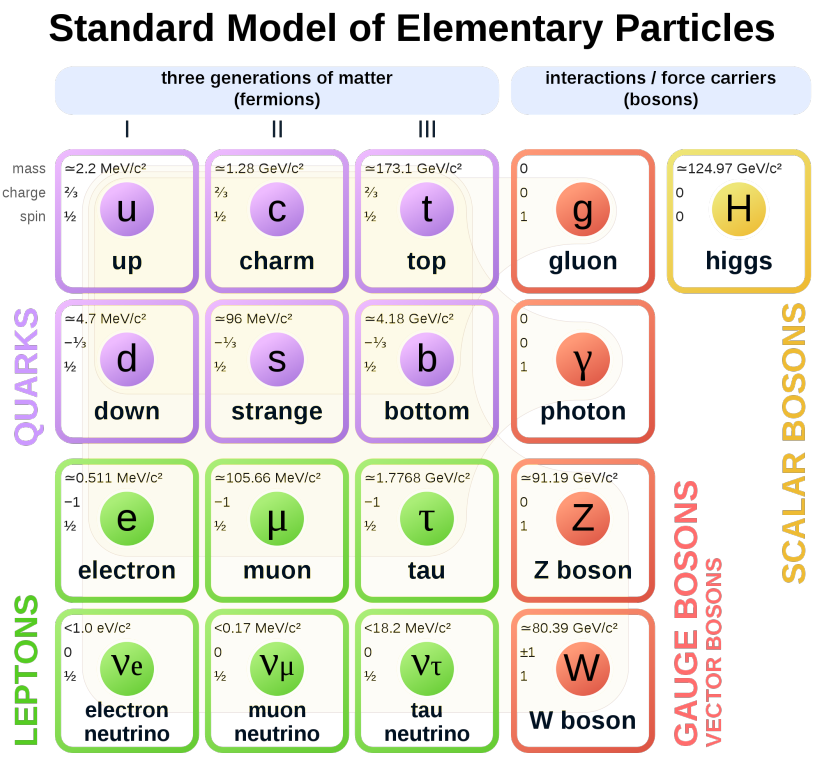

Figure 1: Standard Model of Particle Physics [MC19]

example, they gain in potential energy until it exceeds the rest energy of the quarks that would be needed to build new hadrons. The production of new hadrons by using up potential energy beyond this threshold is aptly called hadronization. Confinement and hadronization can be observed with mesons, consisting of a quark anti-quark pair as illustrated in Fig 2, and baryons, consisting of three quarks of different color.

2.2 K^0_S meson and (anti-) Λ hyperon

K^0_S mesons and $(\bar{\Lambda})\Lambda$ hyperons are hadrons containing either a s or $\bar{s}$ quark [Dem17].

$$|K^0_S> = \frac{1}{\sqrt{2}}|d\bar{s} - s\bar{d}>$$
$$|\Lambda> = |uds>$$
$$|\bar{\Lambda}> = |\bar{u}\bar{d}\bar{s}>$$

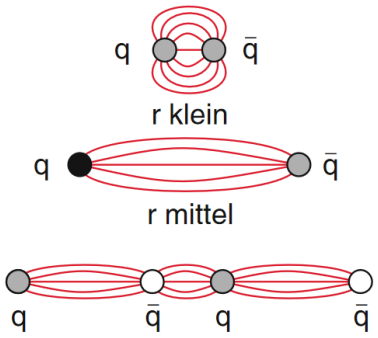

Figure 2: Confinement in mesons [Dem17]

They are instable, have a mean lifetime of $\tau = 0.8954 \times 10^{-10}$ s and $\tau = 2.632 \times 10^{-10}$ s and decay via the weak interaction transforming the s quark. The primary decay channels for K_S^0 mesons and $\Lambda(\bar{\Lambda})$ hyperons are listed below [Gro21a], [Gro21b].

$$
\begin{aligned}
K_S^0 &\rightarrow \pi^+ + \pi^-(69.20\%) \\
K_S^0 &\rightarrow \pi^0 + \pi^0(30.69\%) \\
\Lambda &\rightarrow p + \pi^-(63.9\%) \\
\Lambda &\rightarrow n + \pi^0(35.8\%) \\
\bar{\Lambda} &\rightarrow \bar{p} + \pi^+(63.9\%) \\
\bar{\Lambda} &\rightarrow \bar{n} + \pi^0(35.8\%)
\end{aligned}
$$

2.3 Kinematics in detector physics

At this point a short introduction to some kinematic variables, used in experimental particle physics to describe particle movement in detectors, is given. Basically, a spherical coordinate system with radius r, polar angle θ and azimuthal angle ϕ is used. Transverse momentum p_T is the particle's momentum in the azimuthal plane, thus it can be written as a projection of $|p|$ as in equation 2.

$$p_T = |p| \, cos \, (\theta) \tag{2}$$

Rapidity y is a measure for relativistic velocity and can be defined by using energy and longitudinal momentum p_z as in equation 3.

$$\begin{aligned} y &= artanh\left(\frac{v}{c}\right) \\ &= \frac{1}{2} ln\left(\frac{E + p_z c}{E - p_z c}\right) \end{aligned} \tag{3}$$

The pseudorapidity η 4 is a function of the polar angle θ.

$$\begin{aligned} \eta &= -ln\left[tan\left(\frac{\theta}{2}\right)\right] \\ &= artanh\left(\frac{p_z}{|p|}\right) \end{aligned} \tag{4}$$

As such it gives measure of the angle between a produced particle and the beam axis z. In high energy systems rapidity can be estimated to equal pseudorapidity $y \approx \eta$, which is quite comfortable as only the polar angle is relevant for η.

3 Methods

3.1 Large Hadron Collider

To date the LHC (Large Hadron Collider) of the European Organization for Nuclear Research (CERN), Fig. 3, is the largest synchrotron ever build, accelerating protons, lead (Pb) and xenon (Xe) in a ring spanning 26.7 km in the attempt to expand physical understanding beyond the Standard Model. It delivers pp, p-Pb and Pb-Pb collisions since operation began in 2009. After it was upgraded from 2013 to 2015 it now produces collisions at center-of-mass energies of up to $\sqrt{s} = 13\,\text{TeV}$, $\sqrt{s} = 8.16\,\text{TeV}$ and $\sqrt{s} = 5.02\,\text{TeV}$ respectively. Furthermore, Xe-Xe collisions at up to $\sqrt{s} = 5.44\,\text{TeV}$ were introduced at that point.

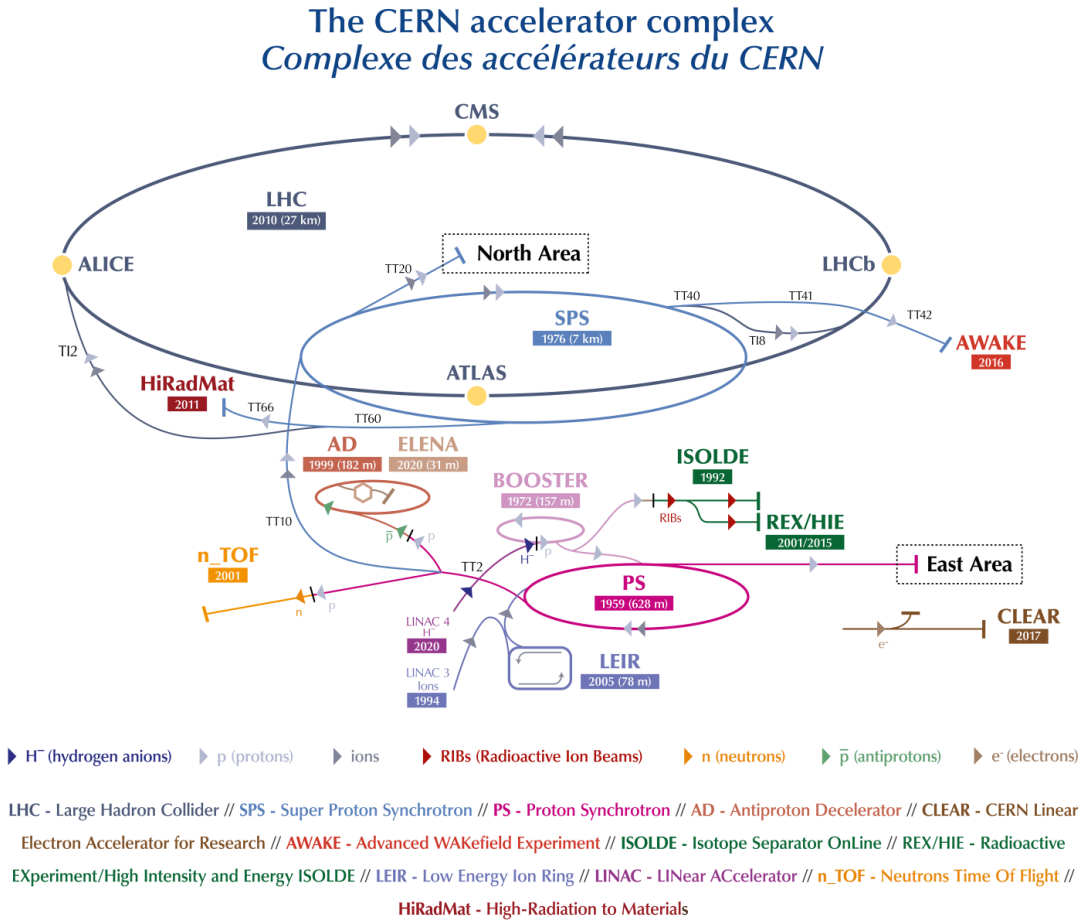

Figure 3: The CERN accelerator complex. [Mob19]

Before entering the main ring, particles gain velocity in smaller accelerators. The LHC itself consists of two beam pipes running magnetically contained particle beams in opposing directions. These two beams are set up to intersect in four different locations on the ring, where the major experiments take place.

- **ATLAS** (A Toroidal LHC ApparatuS)
- **CMS** (Compact Muon Solenoid)
- **LHCb** (Large Hadron Collider beauty)
- **ALICE** (A Large Ion Collider Experiment)

3.2 ALICE

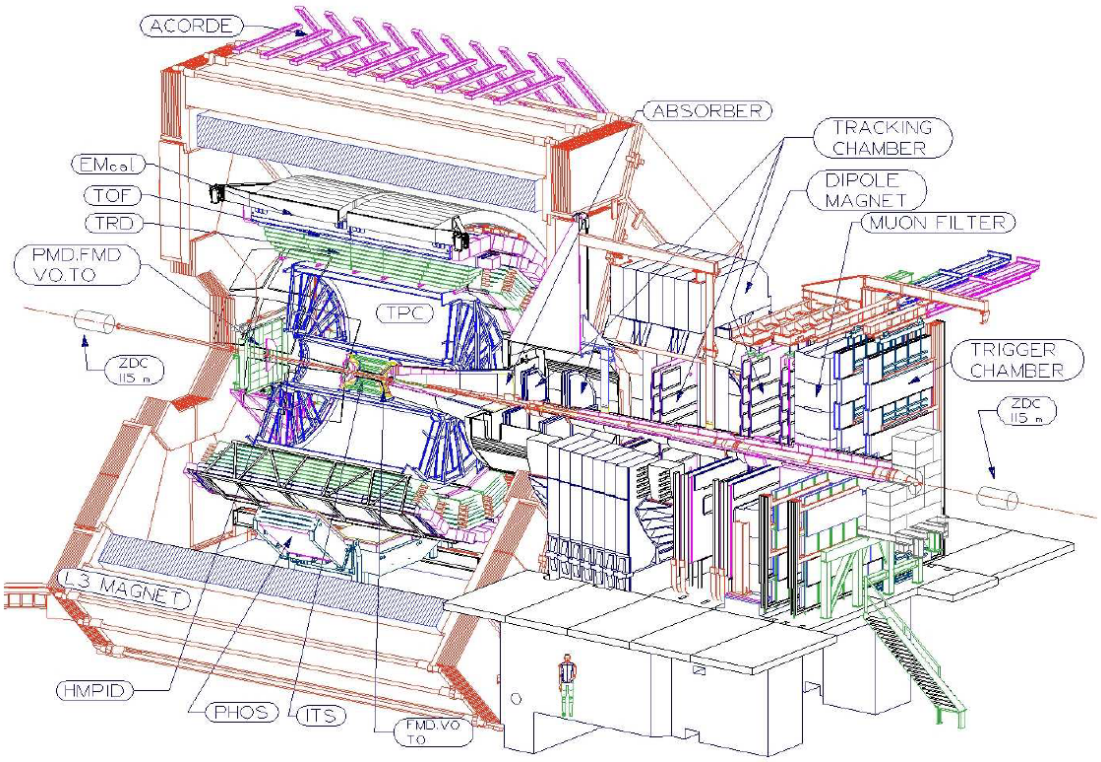

Figure 4: The ALICE detector. [Col+08]

The ALICE apparatus, shown in Fig. 4, is a general-purpose detector, focused on research in heavy ion collisions. The extremely high temperatures und energy density, reached in Pb-Pb collisions at $\sqrt{s} = 5.02\,\text{TeV}$, loosen up the confinement of quarks,

thus enabling research on the quark-gluon-plasma, the state of matter right after the big bang. Even though it is focused on Pb-Pb collisions ALICE adequately observes p-p collisions as well, especially to gain reference data since the basic parton interaction is the same, yet interactions of remaining nucleons do not occur in p-p collisions. ALICE covers an exceptionally large range of transverse momentum for particle detection and identification by layering different systems.

The designed collision point is enclosed by the ITS (Inner Tracking System), a six-layered silicon scintillator, with a radial distance of 3.9 cm, covering the full azimuthal range and the pseudorapidity interval of $-0.9 < \eta < 0.9$. The ITS provides the primary collision vertex, which is the actual point of collision, and secondary decay vertices important to detect heavy flavoured and strange quarks. Furthermore, it improves the resolution of medium and high p_T-measurements and provides low p_T-measurements by itself, [Col+08].

Following the ITS with a distance of 84.8 cm comes the TPC (Time Projection Chamber). Basically the TPC is a 4.994 m long gas ionization chamber with an outer radius of 2.466 m and it is ALICE's primary device for particle identification and tracking. It covers full azimuthal range and pseudorapidity of $-0.9 < \eta < 0.9$ like the ITS. While passing through the gas, particles ionize gas molecules by collision, creating positive ions and free electrons, which drift along the electric field towards the end caps, which are equipped with arrays of multi-wire proportional detection chambers (MWPDCs). While azimuthal direction can be read from which MWPDCs responds, the electron's and ion's time of flight gives the z-coordinates of a particle's path. Thus the crossing particle's path including radius of curvature of its movement in a constant magnetic field and energy loss $\frac{d\mathrm{E}}{dx}$ per path length can be measured, providing its momentum and velocity. These are combined to calculate the particles mass and identify it thereby, [Col+08], [Web18].

Covering the pseudorapidity ranges of $2.8 < \eta < 5.1$ and $-3.7 < \eta < -1.7$ two scintillator arrays, V0A and V0C, are placed on either side of the collision point. The V0 detector provides information on event activity by measuring the multiplicity of primary charged particles. This is also used to reject beam-gas background activity and as a minimum bias trigger for data acquisition, [Col+14].

Additionally the ALICE system contains equipment for the detection of neutral particles, like photons and neutral muons, as well as high energie electrons. This will not be discussed in detail though, as it is not relevant for the experimental contextualization of this thesis.

3.3 PYTHIA

PYTHIA is the established simulation software for high-energy particle collisions, including proton-proton collisions. Programming began in 1978 under the name JETSET. Originally it was written in Fortran but was then rewritten in C++ going from PYTHIA6 to PYTHIA8, v8.306 being the most current release. Using Monte Carlo (MC) methods based on analysis of experimental data and theoretical models, PYTHIA generates collision events as a perfect detector would observe them. To achieve this the complete process is fractioned into a multitude of smaller elementary processes, involving the interaction of only a few particles or simple decays to which stochastic methods are applied. Thus a chain of minor repetitive problems is computed and recorded. "As of version 8.2, the Following processes are available internally:

- **QCD processes** include both soft- and hard-QCD processes. The hard-QCD processes include the standard $2 \to 2$ ones available in PYTHIA6.4, with open charm and bottom production, as well as new $2 \to 3$ processes that can be used, for example, for comparisons with parton showers.
- **Electroweak (EW) processes** include prompt photon production, single production of γ^*/Z and $W^\pm$ as well as pair production of weak bosons with full fermion correlations for $VV \to 4\text{f}$. Photon collision processes of the type $\gamma\gamma \to \text{f}\bar{\text{f}}$ are also available.
- **Onia** include production of any ${}^3S_1$, ${}^3PJ$ and ${}^3DJ$ states of charmonium or bottomonium via colour-singlet and colour-octet mechanisms.
- **Top** production, singly or in pairs.
- **Fourth generation** fermion production via strong or EW interactions.
- **Higgs processes** include the production of the SM Higgs boson as well as the multiple Higgs bosons of a generic two-Higgs-doublet model (2HDM), with the possibility of CP violating decays. It is also possible to modify the angular correlation of the Higgs decay $h \to VV \to 4\text{f}$ due to anomalous hVV couplings. The internal implementation of SUSY also uses the 2HDM implementation for its Higgs sector.
- **SUSY processes** include the pair production of SUSY particles as well as resonant production of squarks via the R-parity violating UDD interaction. EW interferences have been taken into account where relevant and can be turned off for comparisons with PYTHIA6.4. [...] Both squarks and gluinos can be made

to form long-lived R-hadrons, that subsequently decay. In between it is possible to change the ordinary-flavour content of the R-hadrons, by (user-implemented) interactions with the detector material.

- **New gauge boson processes** include production of a Z' (with full $\gamma^*/Z/Z'$ interference), a $W'^{\pm}$ and of a horizontally-coupling (between generations) gauge boson R^0.

- **Left-right symmetric processes** include the production of the $SU(2)_R$ bosons $W_R^{\pm}$, Z_R^0, and the doubly charged Higgs bosons H_L^{++} and H_R^{++}.

- **Leptoquark production** , singly or in pairs, with the assumption that the leptoquark always decays before fragmentation.

- **Compositeness processes** include the production of excited fermions and the presence of contact interactions in QCD or EW processes. The production of excited fermions can be via both gauge and contact interactions; however, only decays via gauge interactions are supported with angular correlation.

- **Hidden Valley processes** can be used to study visible consequences of radiation in a hidden sector. Showering is modified to include a third kind of radiation, fully interleaved with the QCD and QED radiation of the SM. New particles include $SU(N)$ charged gauge bosons as well as partners of the SM fermions charged under $SU(N)$. [...]

- **Extra-dimension processes** include the production of particles predicted by Randall-Sundrum models, TeV-sized and Large Extra Dimensions, and Unparticles. [...]

The full list of available processes and parameters for BSM models along with references is available in the HTML manual distributed with the code." [Sjö+15]

To study physics within and beyond the standard model, event generation is tuned to theoretical predictions and the generated final state is compared to experimental data. For this thesis Pythia is set up for proton-proton collisions at 13 TeV with the Monash 2013 tune. The complete parameter set of the Monash 2013 tune can be found here: [SCR14].

3.4 RIVET

3.4.1 Overview

The RIVET toolkit (Robust Independent Validation of Experiment and Theory) was first released in 2010, the current version being v.3.1.3, and is widely used in the comparison of measurements and theoretical predictions in particle physics. Thus applications of RIVET include, but are not limited to, the development and optimization of MC event generators and as a component of LHCs analysis and interpretation toolkit. "It has been used for development of new analysis techniques including machine learning applications, jet substructure, boosted-particle tagging and pile-up suppression. Extraction of SM parameters for example using TopFitter and other phenomenological studies of the SM have used RIVET, and it has also been employed in searching for and constraining BSM physics, sometimes making use of the related Contur package." [Bie+20b] RIVET does not provide as in depth analyses as ROOT or similar tools but aims to be more user friendly, as RIVET code tends to be self-explanatory, and efficient, in runtime being reduced by caching calculations per event. It is flexible to work with different MC event generators, as long as they provide HepMC format output.

3.4.2 Structure and usage

Fig. 5 lines out the structure of the whole framework. RIVET provides a command line executable that can run a number of included analyses as plugins. This is done with the *rivet* command followed by the analysis name. Furthermore, it provides an extensive library of *C++* functions and a constructor enabling the user to set up and compile individual analyses as new plugins via the *rivet-build* command. The current version of RIVET generates a *.yoda* file to save the analysis output in a readable table-like format. By use of the *rivet-mkhtml* command RIVET creates a figure and *.dat* table for every histogram in the *.yoda* output file and a *html* to browse them comfortably.

Since the goal of this thesis is to create a new analysis the programmatic components shall be discussed further. Every RIVET analysis is composed of three methods: *init()*, *analyze()* and *finalize()*, see Fig 6.

init()

The *init()* method is called once at the beginning of every analysis. Here the observed physics is set up by declaring the *projections* that will be applied per event in the *analyze()* method. Moreover, the histograms to be filled in the *analyze()* method are

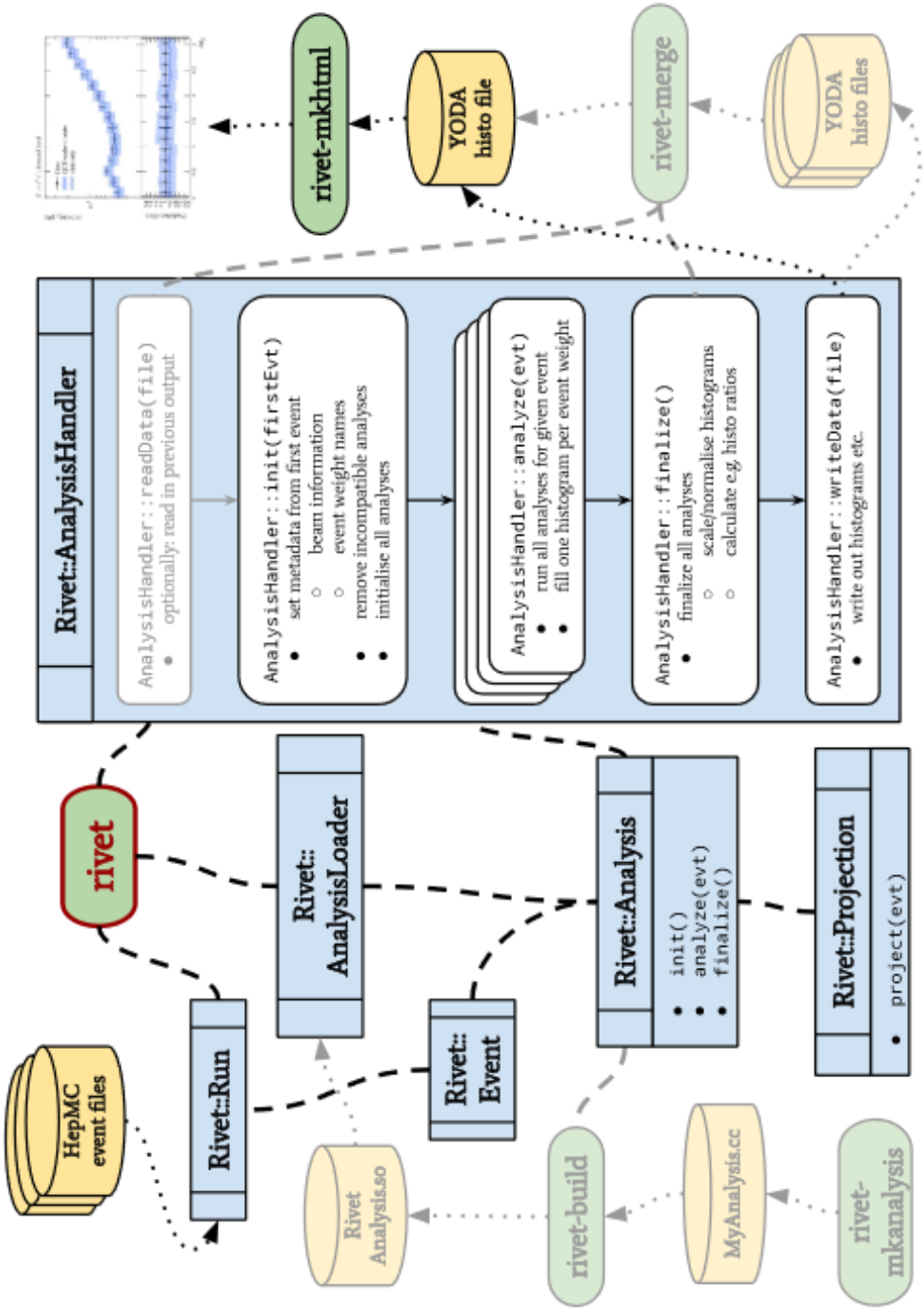

Figure 5: The RIVET systems commands (green), components (blue) and dataflow. Grayed modules are optional to use. User data and code are coloured yellow. [Bie+20b]

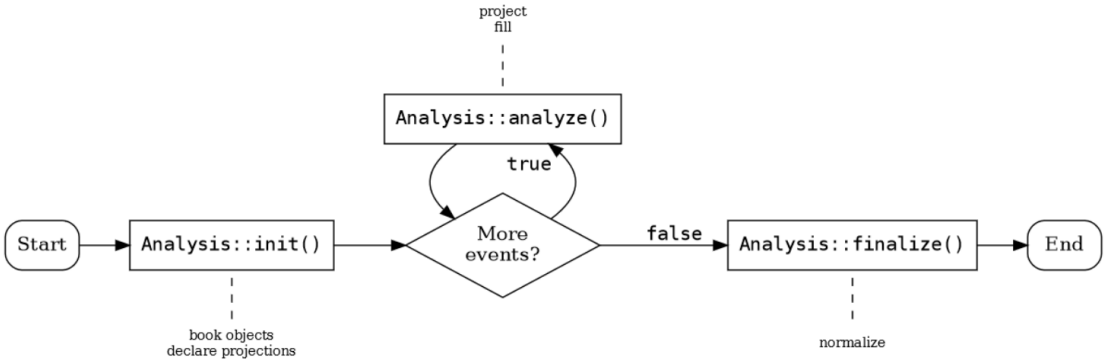

Figure 6: Flowchart of a RIVET analysis. [Bie+20a]

booked here.

analyze()

The *analyze()* method is called for every event. In this method the set *projections* are applied to each event to do the actual calculations and the results are filled into the booked histograms.

finalize()

The *finalize()* method is called once at the end of every analysis to scale, modify or otherwise use the filled histograms for further calculations.

Having already been mentioned, the most important objects in user level programming are histograms and *projections*.

projections

Projections offer easy access to calculations of physical observables to the regular RIVET user as they render most directly written *C++* unnecessary. They can be modified by *Cuts* to put in restrictions, e.g. the *ChargedFinalState projection*, which delivers every charged-hadron that would be detected in a physical detector, can be modified to only deliver particles within a certain pseudorapidity range. As *projections* have to be registered in the *init()* method and are then applied in the *analyze()* method, general *Cuts* can be added in the former and more specific ones in the later. Thereby the exemplary *ChargedFinalState projection* could be set up at registration to filter for protons and then modified at application for groups of protons with specific transverse

momenta. Computationally *projections* offer another feat. They are cached for each event, thus runtime can be reduced significantly if different observables are calculated from the same *projection* by avoiding repeated calculations.

histograms

Histograms are diagrams to approximate probability distributions numerically. They are constructed by dividing the desired range of values into adjacent intervals called bins and filling them by counting the value entries within their respective intervals. In RIVET histograms are set up using the *book()* function, this includes: range of values, bin count, object reference and name. Because many MC event generators allow to generate weighted events, that are biased to specific processes, RIVET allows to fill histograms with weighted values to regain comparability of data. A special peculiarity to RIVET however is that every entry to a bin is normalized to the bins width. In arbitrary units this means that an entry with the weight 1 will be written as the value 10 to a bin with a width of 0.1.

4 Analysis

Objective of this thesis is programming of a RIVET analysis corresponding to the data analysis discussed in the paper **"$\mathbf{K^0_S}$- and (anti-)Λ-hadron correlations in pp collisions at $\sqrt{s} = 13\,\mathrm{TeV}$"** [Col21]. As the RIVET analysis and PYTHIA simulation are independent, the plugin generated from the analysis can be used to verify new parameters for PYTHIA. The paper entails the study of two-particle correlations in pseudorapidity and azimuthal angle, focused on strangeness and multiplicity related effects in hadronization. Since this is done in a rather low range of transverse momentum and in full azimuthal cover, the analysed experimental data is taken from the ALICE experiment. The events analysed in this thesis were generated with PYTHIA set to the Monash 2013 tune. Later on they are compared to the experimental data.

4.1 Multiplicity Selection

The minimum bias trigger of the V0A und V0C detectors was applied to the experimental data, see section 3.2. Furthermore, the event activity was measured and based thereon the events were allocated to six classes (namely: 0-1%, 1-3%, 3-7%, 7-15%, 15-50%, 50-100%). Whereas the 1% of all events with the highest activity was allocated to the 0-1% class and the 50% with the lowest activity were allocated to the 50-100% class. Precisely the classes ranges corrected for detector precision are 0-0.92%, 0.92-2.74%, 6.40-13.44%, 13.44-46.12%, 46.12-100% [Col21]. Additionally, there is a seventh class where every event is allocated. This class is named MB and at this point it represents the sum of the former six. Calculations on this class naturally produce an average.

The RIVET framework includes a projection to calculate ALICEs V0 detector's response comfortably. Thus categorization of events as discussed is easily reproduced in the RIVET analysis.

4.2 Correlations

Subject of this analysis are two-particle correlations of a trigger and associated particle. As trigger particle either a strange particle, namely a $\mathrm{K^0_S}$ or $(\bar{\Lambda})\Lambda$, or a charged-hadron with $3\,\mathrm{GeV} < p_T^{trigg} < 20\,\mathrm{GeV}$ is selected. Associated particles are any charged-hadrons in the event with a transverse momentum within $1\,\mathrm{GeV} < p_T^{assoc} < p_T^{trigg}$. "Since the Λ-h and $\bar{\Lambda}$-h correlation functions are compatible, as expected for this collision energy, the results are combined and reported in the following as $(\Lambda + \bar{\Lambda})$-h." [Col21] Therefore, three groups of correlation functions are explored: h-h, $\mathrm{K^0_S}$-h and $(\Lambda + \bar{\Lambda})$-h. The ALICE experiment detects charged-hadrons with the ITS and TPC, see section 3.2, therefore

the pseudorapidity cannot exceed $|\eta| < 0.9$. In the actual analysis, charged-hadrons are selected within $|\eta| < 0.8$ whereas K^0_S and $(\bar{\Lambda})\Lambda$ are selected within the rapidity range $|y| < 0.5$. For every pair the difference in pseudorapidity and azimuthal angle is calculated and an entry with the weight of 1 is made in a corresponding two-dimensional histogram.

4.3 Transverse Momentum Selection

To study the dihadron correlation functions, the groups, already defined by trigger particle and event activity are further broken down into different ranges of trigger particle transverse momentum p_T^{trigg}. Therefore each correlation is allocated one of eight intervals: $3\,\mathrm{GeV} < p_T^{trigg} < 4\,\mathrm{GeV}$, $4\,\mathrm{GeV} < p_T^{trigg} < 5\,\mathrm{GeV}$, $5\,\mathrm{GeV} < p_T^{trigg} < 6\,\mathrm{GeV}$, $6\,\mathrm{GeV} < p_T^{trigg} < 7\,\mathrm{GeV}$, $7\,\mathrm{GeV} < p_T^{trigg} < 9\,\mathrm{GeV}$, $9\,\mathrm{GeV} < p_T^{trigg} < 11\,\mathrm{GeV}$, $11\,\mathrm{GeV} < p_T^{trigg} < 15\,\mathrm{GeV}$, $15\,\mathrm{GeV} < p_T^{trigg} < 20\,\mathrm{GeV}$. Since the total energy in the event is limited to the collision energy by energy conservation, an increase in overall particle (transverse) momentum is conterminous to a decrease in particle multiplicity. The energy transfer between them is conveyed by processes like colour string fragmentation and colour string reconnection.

Eventually, this leads to a total number of $3 \cdot 7 \cdot 8 = 168$ basic correlation functions and corresponding histograms depicting them. This number is further increased by breaking the MB group down in yet another way, as the $p_T^{trigger}$ selection is subdivided by a p_T^{assoc} selection with ten intervals $1\,\mathrm{GeV} < p_T^{assoc} < 2\,\mathrm{GeV}$, $2\,\mathrm{GeV} < p_T^{assoc} < 3\,\mathrm{GeV}$, $3\,\mathrm{GeV} < p_T^{assoc} < 4\,\mathrm{GeV}$, $4\,\mathrm{GeV} < p_T^{assoc} < 5\,\mathrm{GeV}$, $5\,\mathrm{GeV} < p_T^{assoc} < 6\,\mathrm{GeV}$, $6\,\mathrm{GeV} < p_T^{assoc} < 7\,\mathrm{GeV}$, $7\,\mathrm{GeV} < p_T^{assoc} < 9\,\mathrm{GeV}$, $9\,\mathrm{GeV} < p_T^{assoc} < 11\,\mathrm{GeV}$, $11\,\mathrm{GeV} < p_T^{assoc} < 15\,\mathrm{GeV}$ and $15\,\mathrm{GeV} < p_T^{assoc} < 20\,\mathrm{GeV}$. Considering $p_T^{assoc} < p_T^{trigg}$, this adds 156 valid correlation functions and histograms to the analysis.

4.4 Per Trigger Normalization

The 324 stated histograms count every two-particle correlation and are therefore dependent on the size of the dataset. For this reason each histogram is complemented by a trigger particle counter, enabling the normalization to an average per trigger particle count, Fig. 7a.

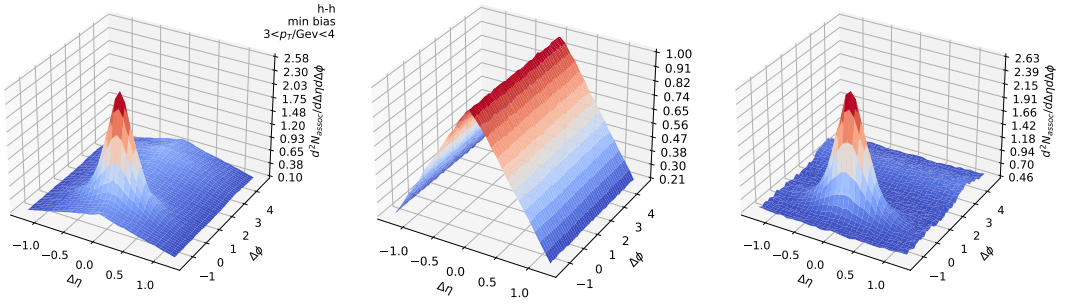

(a) (b) (c)

Figure 7: Example of a two-particle correlation function per trigger particle (a), mixed-event two-particle correlation function (b) and efficiency-corrected correlation function (c).

4.5 Correction - Mixed Event Method

Correlating two particles within $|\eta| < 0.8$ in η creates a bias towards a triangular distribution around zero. To compensate for this - and irregular detector efficiency with the ALICE data - the mixed-event method is applied, wherein two particles of different events are correlated. In this manner no physical correlation is possible and only methodic and systematic effects remain. The mixed-event correlation function is normalized to one, Fig. 7b, and the per-trigger average, Fig. 7a is divided by this, resulting in the corrected correlation function, Fig. 7c.

4.6 Projection on azimuthal angle

In Fig. 7c a clear peak can be seen in $\Delta\eta = 0$ and $\Delta\phi = 0$ and another in $\Delta\phi = \pi$, smeared in $\Delta\eta$, can be suspected as well. The next step is a dimension-reducing integration in $|\Delta\eta| < 1$, projecting the correlation function on $\Delta\phi$. This is followed by a subtraction of the underlying background with the ZYAM (Zero Yield At Minimum) method, whereas "the background is estimated to be the average value of six bins outside the jet peaks to reduce the statistical fluctuations." [Col21]
The one-dimensional correlation function, Fig. 8, shows the second peak in $\Delta\phi$ clearly. This matches theoretical expectations, since the presumption of a connection in the production of trigger and associated particle legitimates this analysis and daughter particle momentum sums to mother particle momentum, which leads for example to contrariwise orientation of two particles momenta in two-particle decays.

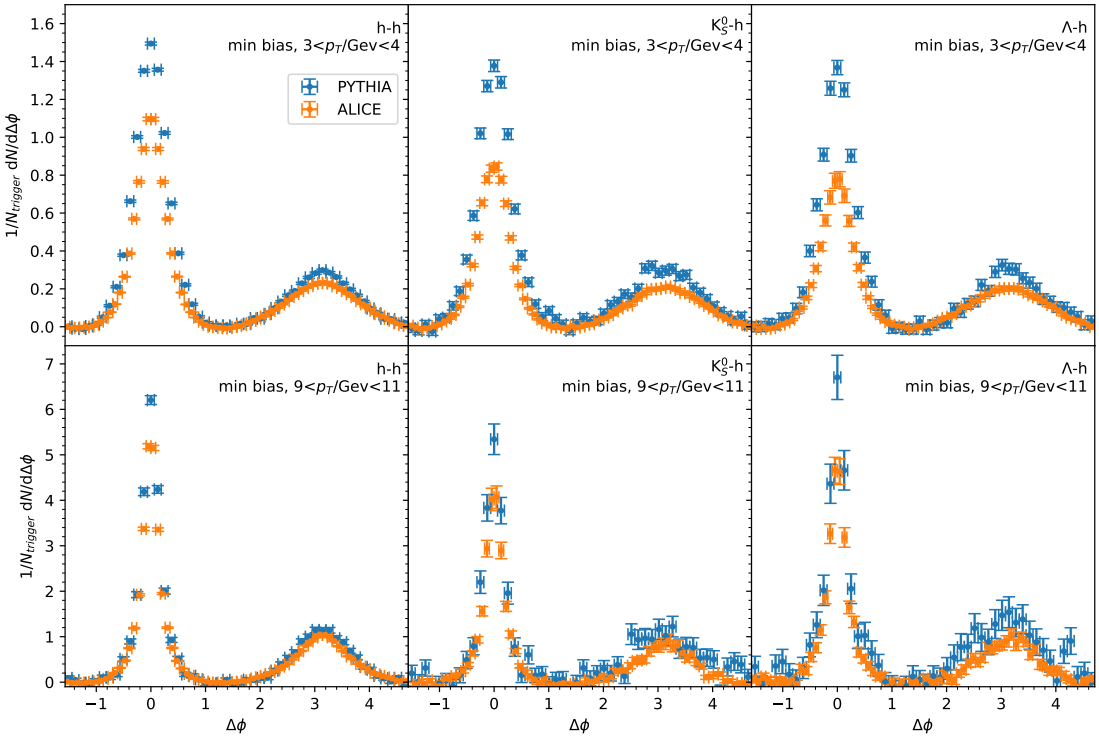

Figure 8: One-dimensional correlation function generated with a $\Delta\phi$ projection of the two-dimensional correlation function, Fig. 7c, reduced of event background with the ZYAM method. ALICE data taken from HepData, corresponding to [Col21].

4.7 Peak Yields

Eventually the one-dimensional correlation functions are integrated within the intervals $|\Delta\phi| < 0.9$ and $|\Delta\phi - \pi| < 1.4$ to get the near- and away-side per-trigger yields. They are then plotted over multiplicity class and trigger-particle transverse momentum $p_T^{trigger}$ or $p_T^{trigger}$ and associated-particle transverse momentum p_T^{assoc} to search for trends.

4.8 Uncertainties

Because the RIVET analysis runs on simulated data, uncertainties originate from statistics, determined by the number of events analyzed, and systematic sources like bin sizes. Therefore, uncertainties in integrated per-trigger yields originate from the two-dimensional correlation functions by error propagation, whereas the integration over neighboring bins comes with the calculation of uncertainty as the geometric mean value of the bin's uncertainties. The uncertainty on integration intervals is less straight forward

though. Eventually, the analysis will run with 72 bins in azimuthal angle and 49 bins in pseudorapidity, resulting in a bin size of $b_{\Delta\phi} = \frac{2\cdot\pi}{72} = 0.0873 \times b_{\Delta\eta} = \frac{1.32}{49} = 0.0269$. The integration in $|\eta| < 1$ thus will come with an uncertainty $u_{\Delta\eta} = 0.0381$ and in $|\Delta\phi| < 0.9$ ($|\Delta\phi - \pi| < 1.4$) with an uncertainty of $u_{\Delta\phi} = 0.1234$. As of now, the analysis has only been run with a reduced count of bins to cut on runtime, 50 bins in azimuthal angle and 31 bins in pseudorapidity, resulting in uncertainties of $u_{\Delta\eta} = 0.0602$ and $u_{\Delta\phi} = 0.1777$.

5 Results and Discussion

In the one-dimensional correlation function for minimum bias, $3\,\mathrm{GeV} < p_T^{trigger} < 4\,\mathrm{GeV}$ and $9\,\mathrm{GeV} < p_T^{trigger} < 11\,\mathrm{GeV}$, Fig. 8, we see that PYTHIA, in the given setup, overestimates the production of associated particles for every given trigger particle in the near-side peak significantly. The away-side peak is better modelled, as there associated particle count is only slightly overestimated. Furthermore, the uncertainties indicate that K^0_S-h and $(\Lambda+\overline{\Lambda})$-h correlations need to be researched based on a bigger dataset to gain as statistically meaningful results as from the h-h correlations. This demand shows a trend increasing with trigger particle transverse momentum $p_T^{trigger}$. Actually both observations are sensible, as K^0_S mesons and $(\overline{\Lambda})\Lambda$ hyperons are obviously produced with a lower probability than any unidentified charged-hadron and an increase in particle momentum is generally conterminous to particle production. Nonetheless, this demand for higher statistics has an impact on the following results and their discussion. At this stage the RIVET plugin was only run on a dataset of 8 million events and with decreased bin sizes, see 4.8, to reduce runtime demand as it was not run on a cluster yet. As such, results and discussion focus on verifying whether the analysis performs as intended and physical observations are mostly derived exemplary from the paper.

5.1 Per-trigger Yields

Figure 9 illustrates the per-trigger yields as a function of trigger particle transverse momentum $p_T^{trigger}$. As expected, since higher energetic jets generally include more particles [Col21], an increase in associated particle count with $p_T^{trigger}$ can be observed for all three correlations on the near-side and the far-side for h-h. For the far-side of K^S_0-h and $(\overline{\Lambda})\Lambda$-h correlations the same trend can be suspected, yet the lack of sufficient statistics impedes a conclusive observation.

Multiplicity dependence of the per-trigger yields is researched by calculating the ratio to the minimum bias class for the different activity classes. Here the low statistics become problematic, as there cannot be any trend derived from Fig. 10 with uncertainties bigger than the actual values. A close inspection of the per-trigger yields, Fig. 9, already hints at this with the increase of peak yield over $p_T^{trigger}$ being irregular, even for the near-side h-h correlations.

Figure 11, taken from the paper [Col21], illustrates the same ratio for the data from ALICE. Here a trend can be observed for both peaks in the h-h correlations. Events

with higher activity, showing the higher associated particle count for the near-side peak, which is quite conclusive. The increase in $p_T^{trigger}$ leads to an asymptotic trend towards the minimum bias class, which is the average, for all event-activity classes. For the away-side peak the first observation can be made with low $p_T^{trigger}$ as well, but the increase in $p_T^{trigger}$ leads to the peak yields diverging from average. This can be explained with a bias for jets to smear in η with growing transverse momentum. Therefore, the probability of associated particles not being within η acceptance is increased for high multiplicity classes.

The per-trigger yields as a function of p_T^{assoc} for min. bias, Fig. 12, exhibits a decreasing trend, which again can be seen best for the h-h correlations. This coincides with expectations, as the increase in p_T^{assoc} decreases the probability of the associated particles actual production. Furthermore, an increase in associated particle count with $p_T^{trigger}$ can be observed, which compliments the observations made on the per-trigger yields as a function of $p_T^{trigger}$, Fig. 9.

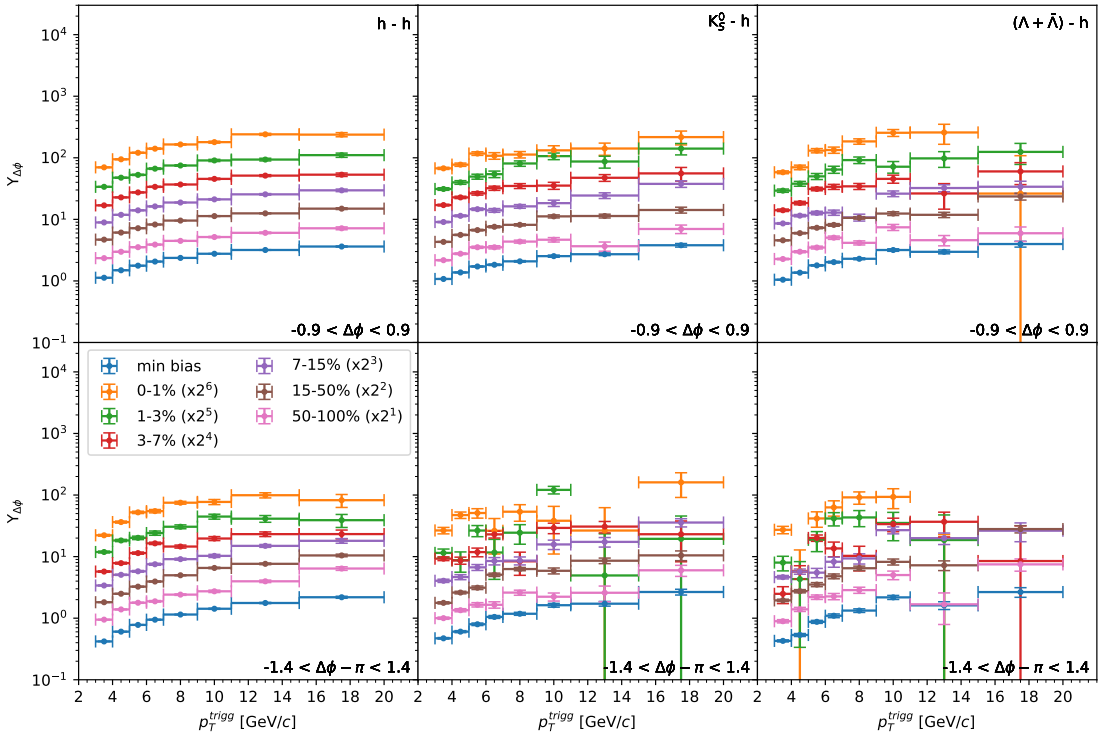

Figure 9: Per-trigger yields of two-particle correlations as a function of $p_T^{trigger}$. Near-side peak in the upper row, away-side peak in the lower row for h-h (left), K^0_S-h (middle), $(\Lambda+\overline{\Lambda})$-h (right) correlations.

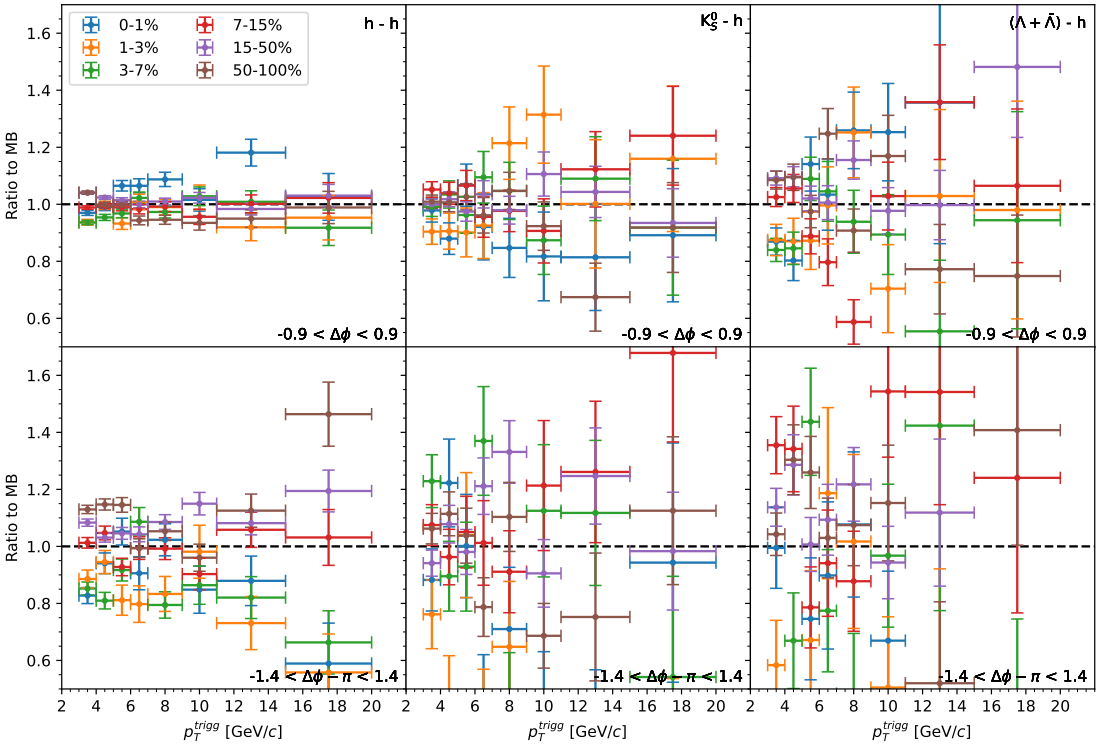

Figure 10: Per-trigger yield ratio to min. bias of different multiplicity classes as a function of $p_T^{trigger}$. Near-side peak in the upper row, away-side peak in the lower row for h-h (left), K^0_S-h (middle), $(\Lambda + \overline{\Lambda})$-h (right) correlations.

5.2 Comparison with experimental data

In the long term this part is the most important aspect of this thesis. Remember, that the development of the corresponding RIVET analysis was motivated by the wish for a tool to verify the adjustment of parameters in PYTHIA to fit ALICE data and explore the physical processes involved in hadronization. Therefore, the ratio of PYTHIA simulation and ALICE data will be important when the analysis is actually used. Figure 13 illustrates this ratio for the correlations as functions of $p_T^{trigger}$. In case of the h-h correlations it gives conclusive and quantitative results, indicating that PYTHIA systematically overestimates associated particle production for low $p_T^{trigger}$ range by factor of 1.1 to 1.7. This compliments and quantifies the obvious observation on figure 8. For the K^0_S-h and $(\Lambda + \overline{\Lambda})$-h correlations, such conclusions can not be derived at this point. Nonetheless, they were included in Fig. 13, because they can be essential when using the analysis to tune PYTHIA, based on a bigger dataset.

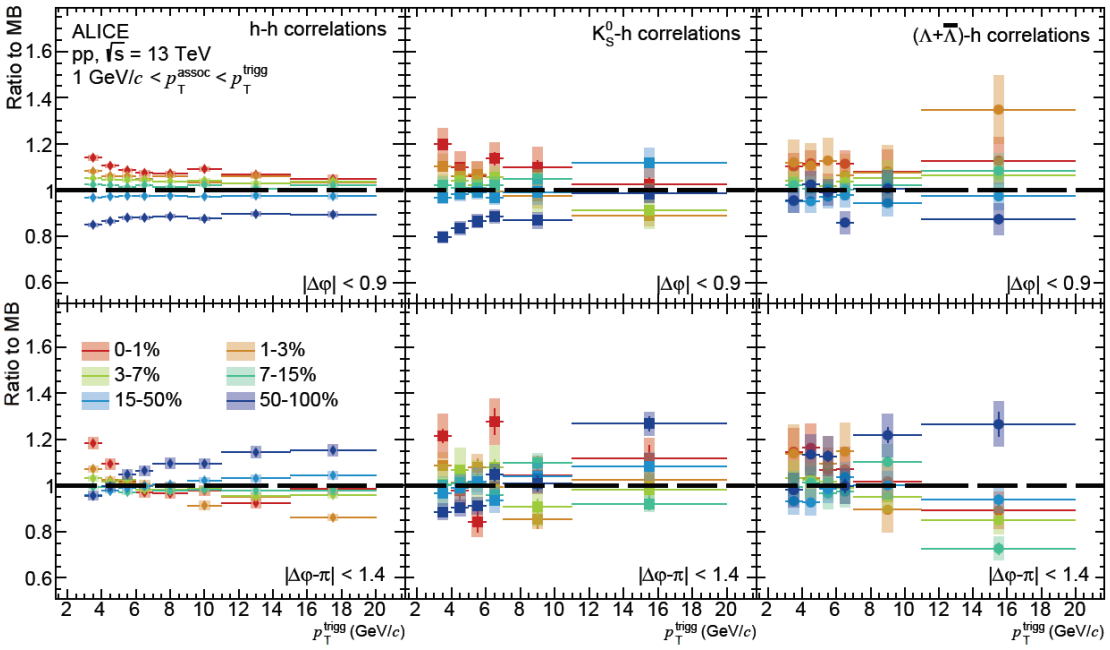

Figure 11: Per-trigger yield ratio to min. bias of different multiplicity classes as a function of $p_T^{trigger}$, ALICE. Near-side peak in the upper row, away-side peak in the lower row for h-h (left), K_S^0-h (middle), $(\Lambda + \overline{\Lambda})$-h (right) correlations. [Col21]

The ratio for the correlations as functions of p_T^{assoc} can be of use at a later stage as well, but are only included in the appendix, as no physical conclusions can be derived from them at this point.

5.3 Comparison of Hadron- and Strangeness-Triggered Yields

This section is included, because quantifying the bias the participation of a strange quark puts on production of associated particles is one of the main objectives of the paper that motivated this thesis. Since the statistics on K_S^0-h and $(\Lambda + \overline{\Lambda})$-h correlations are not sufficient to draw any conclusion about the adequacy of the PYTHIA simulation, only the general trend is discussed briefly based on the ALICE data from the paper. Figure 14 illustrates the ratios of K_0^S-h and $(\Lambda + \overline{\Lambda})$-h to h-h per-trigger yields as a function of $p_T^{trigger}$ for ALICE and PYTHIA. A corresponding figure depicting the ALICE data and the PYTHIA predictions analysed with RIVET is included in the appendix. For the near-side it can be observed, that the yield ratios $Y_{\Delta\phi}^{K_S^0-h}$ / $Y_{\Delta\phi}^{h-h}$ are below unity and constant with $p_T^{trigger}$. This applies to all multiplicity classes without significant

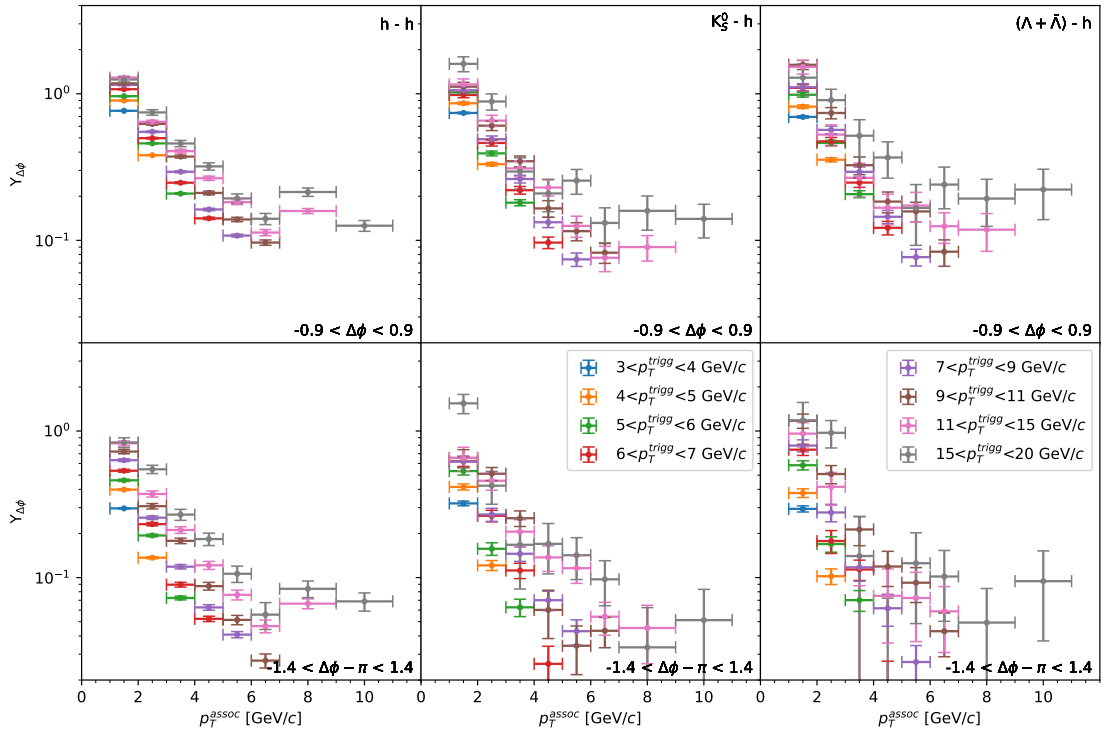

Figure 12: Per-trigger yields of two-particle correlations as a function of p_T^{assoc} for min. bias. Near-side peak in the upper row, away-side peak in the lower row for h-h (left), K^0_S-h (middle), $(\Lambda+\overline{\Lambda})$-h (right) correlations. Because of $1\,\text{GeV} < p_T^{assoc} < p_T^{trigger}$ the full range of p_T^{assoc} is not covered for every $p_T^{trigger}$.

irregularity indicating, that the participation of a K^0_S meson biases the event towards a lower associated particle, production independently of $p_T^{trigger}$ or multiplicity. The $Y_{\Delta\phi}^{(\Lambda+\overline{\Lambda})-h}$ / $Y_{\Delta\phi}^{h-h}$ on the other hand shows an increase with $p_T^{trigger}$. "Potentially, this could be explained with a bias towards gluon jets, which contain more particles and have a relative enhanced production of Λ hyperons." [Col21] At a later stage the implemented Rivet analysis can be used to explore the reasons behind this and other observations, by applying it to Pythia set up for different processes and evaluating their respective results.

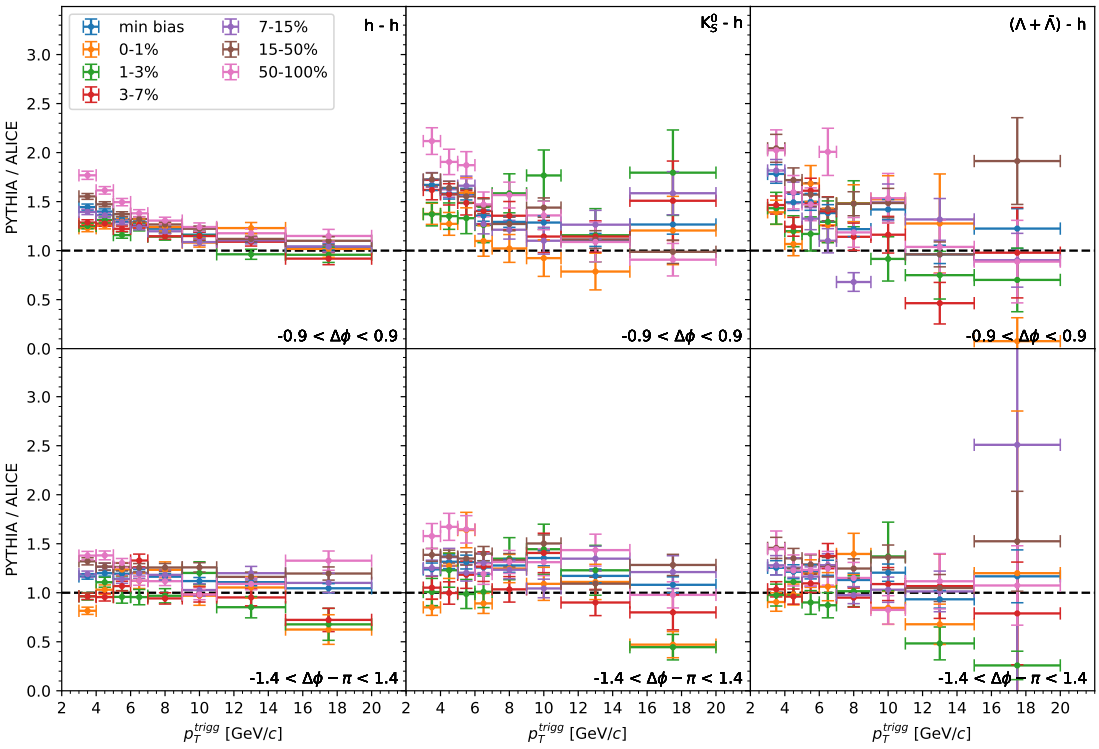

Figure 13: Ratio of PYTHIA to ALICE of per-trigger yields as a function of $p_T^{trigger}$. Near-side peak in the upper row, away-side peak in the lower row for h-h (left), K^0_S-h (middle), $(\Lambda + \overline{\Lambda})$-h (right) correlations.

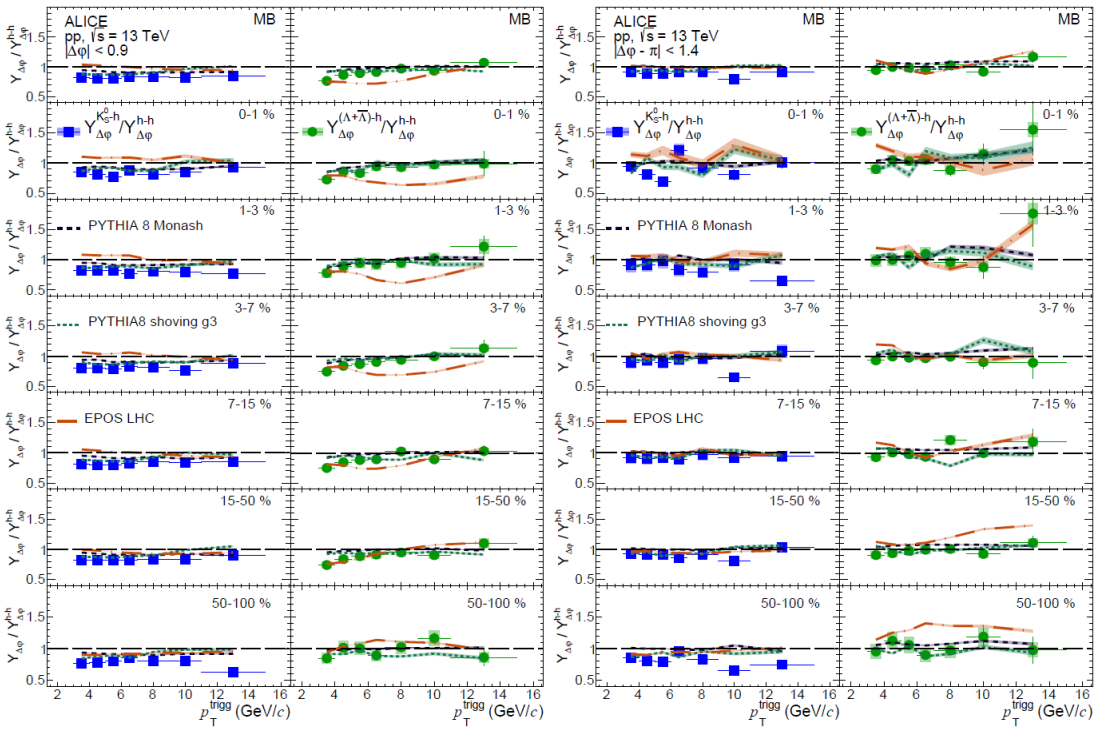

Figure 14: Ratios of K^S_0-h and $(\Lambda+\overline{\Lambda})$-h to h-h per-trigger yields as a function of $p_T^{trigger}$. [Col21]

6 Conclusion and Outlook

The main objective of this thesis was to supplement the paper "**K^0_S- and (anti-) Λ-hadron correlations in pp collisions at $\sqrt{s} = 13\,\text{TeV}$**" [Col21] with a RIVET analysis. Eventually, it can be used to tune PYTHIA to the ALICE data on K^0_S-h and $(\overline{\Lambda})\Lambda$-h correlations and explore the machinations behind the bias a strange quark exerts on charged-hadron production.

As such, the RIVET analysis correlates charged-hadrons, K^0_S and $(\overline{\Lambda})\Lambda$ hyperons within $3\,\text{GeV} < p_T^{trigger} < 20\,\text{GeV}$ with associated charged-hadrons within $1\,\text{GeV} < p_T^{assoc} < p_T^{trigger}$ in the dihadron correlation approach and calculates the near-side and away-side per-trigger yield. This is done separately for different event-activity classes as well as different p_T^{assoc} and $p_T^{trigger}$ intervals to further explore multiplicity and momentum related effects and compared to ALICE data.

At this stage the increase of associated particle count for all multiplicity classes with trigger particle momentum can be observed in figure 9. The effect of event-activity was examined in figure 10, but the lack of statistical significance prohibits conclusions. Nonetheless, the functionality of the analysis in this regard is backed up by comparisons with the paper [Col21] in low $p_T^{trigger}$ range of the h-h correlations. Furthermore, the systematic overestimation of associated particle production on the near-side by the given PYTHIA setup becomes clear in figure 13, especially for the h-h correlations, as they are again of the most statistical significance. Effects of associated particle momentum p_T^{assoc} on associated particle count are visible in figure 12, where the decrease in peak-yield with increase of p_T^{assoc} is visible. This aspect could not be researched further at this point though, as it proves to be even more dependent on a sufficient number of events to become sensible. Finally, the effect of the participation of strange quarks in the event on the production of charged-hadrons could not yet be explored based on this analysis. At a later stage though, with the analysis running on a cluster to process billions of events, it should allow for this, as functionality is implied by the current results.

List of Figures

1 Standard Model of Particle Physics 8
2 Confinement in mesons 9
3 The CERN accelerator complex 11
4 The ALICE detector 12
5 The RIVET System 17
6 RIVET analysis flowchart 18
7 Two-dimensional correlation function. 22
8 One-dimensional correlation function. 23
9 Per-trigger yields of two-particle correlations as a function of $p_T^{trigger}$. . . . 26
10 Per-trigger yield ratio to min. bias of different multiplicity classes as a function of $p_T^{trigger}$. 27
11 Per-trigger yield ratio to min. bias of different multiplicity classes as a function of $p_T^{trigger}$, ALICE. 28
12 Per-trigger yields of two-particle correlations as a function of p_T^{assoc} for min. bias. 29
13 Ratio of PYTHIA to ALICE of per-trigger yields as a function of $p_T^{trigger}$. . 30
14 Ratios of K_0^S-h and $(\Lambda + \overline{\Lambda})$-h to h-h per-trigger yields as a function of $p_T^{trigger}$. 31
15 Ratio of PYTHIA to ALICE of per-trigger yields for min. bias as a function of p_T^{assoc}. 35
16 Ratios of K_0^S-h and $(\Lambda + \overline{\Lambda})$-h to h-h per-trigger yields as a function of $p_T^{trigger}$. 36

References

[Col+08] The ALICE Collaboration et al. "The ALICE experiment at the CERN LHC". In: *Journal of Instrumentation* 3.08 (Aug. 2008), S08002–S08002. DOI: 10.1088/1748-0221/3/08/s08002. URL: https://doi.org/10.1088/1748-0221/3/08/s08002.

[Col+14] The ALICE Collaboration et al. "Performance of the ALICE experiment at the CERN LHC". In: *International Journal of Modern Physics A* 29.24 (Sept. 2014), p. 1430044. ISSN: 1793-656X. DOI: 10.1142/s0217751x14300440. URL: http://dx.doi.org/10.1142/S0217751X14300440.

[Pov+14] Bogdan Povh et al. *Teilchen und Kerne - Eine Einführung in die physikalischen Konzepte*. Springer, 2014. ISBN: 9783642378218.

[SCR14] P. Skands, S. Carrazza, and J. Rojo. "Tuning PYTHIA 8.1: the Monash 2013 tune". In: *The European Physical Journal C* 74.8 (Aug. 2014). ISSN: 1434-6052. DOI: 10.1140/epjc/s10052-014-3024-y. URL: http://dx.doi.org/10.1140/epjc/s10052-014-3024-y.

[Sjö+15] Torbjörn Sjöstrand et al. "An introduction to PYTHIA 8.2". In: *Computer Physics Communications* 191 (June 2015), pp. 159–177. ISSN: 0010-4655. DOI: 10.1016/j.cpc.2015.01.024. URL: http://dx.doi.org/10.1016/j.cpc.2015.01.024.

[Dem17] Wolfgang Demtröder. *Experimentalphysik 4*. Springer, 2017. ISBN: 9783662528846.

[Web18] Steffen Weber. "Multiplicity dependent J/psi production in proton-proton collisions at the LHC". In: (2018).

[MC19] Wikipedia authors MissMJ and Cush. *Standard Model of Elementary Particles*. 2019. URL: https://en.wikipedia.org/wiki/File:Standard_Model_of_Elementary_Particles.svg.

[Mob19] Esma Mobs. "The CERN accelerator complex - 2019. Complexe des accélérateurs du CERN - 2019". In: (July 2019). General Photo. URL: https://cds.cern.ch/record/2684277.

[Bie+20a] Christian Bierlich et al. "Confronting experimental data with heavy-ion models: Rivet for heavy ions". In: *The European Physical Journal C* 80.5 (May 2020). ISSN: 1434-6052. DOI: 10.1140/epjc/s10052-020-8033-4. URL: http://dx.doi.org/10.1140/epjc/s10052-020-8033-4.

[Bie+20b] Christian Bierlich et al. "Robust Independent Validation of Experiment and Theory: Rivet version 3". In: *SciPost Physics* 8.2 (Feb. 2020). ISSN: 2542-4653. DOI: 10.21468/scipostphys.8.2.026. URL: http://dx.doi.org/10.21468/SciPostPhys.8.2.026.

[Col21] ALICE Collaboration. *K^0_S- and (anti-)Λ-hadron correlations in pp collisions at $\sqrt{s} = 13$ TeV*. 2021. arXiv: 2107.11209 [nucl-ex].

[Gro21a] Particle Data Group. 2021. URL: https://pdg.lbl.gov/2021/web/viewer.html?file=%2F2021/tables/rpp2021-sum-baryons.pdf.

[Gro21b] Particle Data Group. 2021. URL: https://pdg.lbl.gov/2021/web/viewer.html?file=%2F2021/tables/rpp2021-sum-mesons.pdf.

Appendix

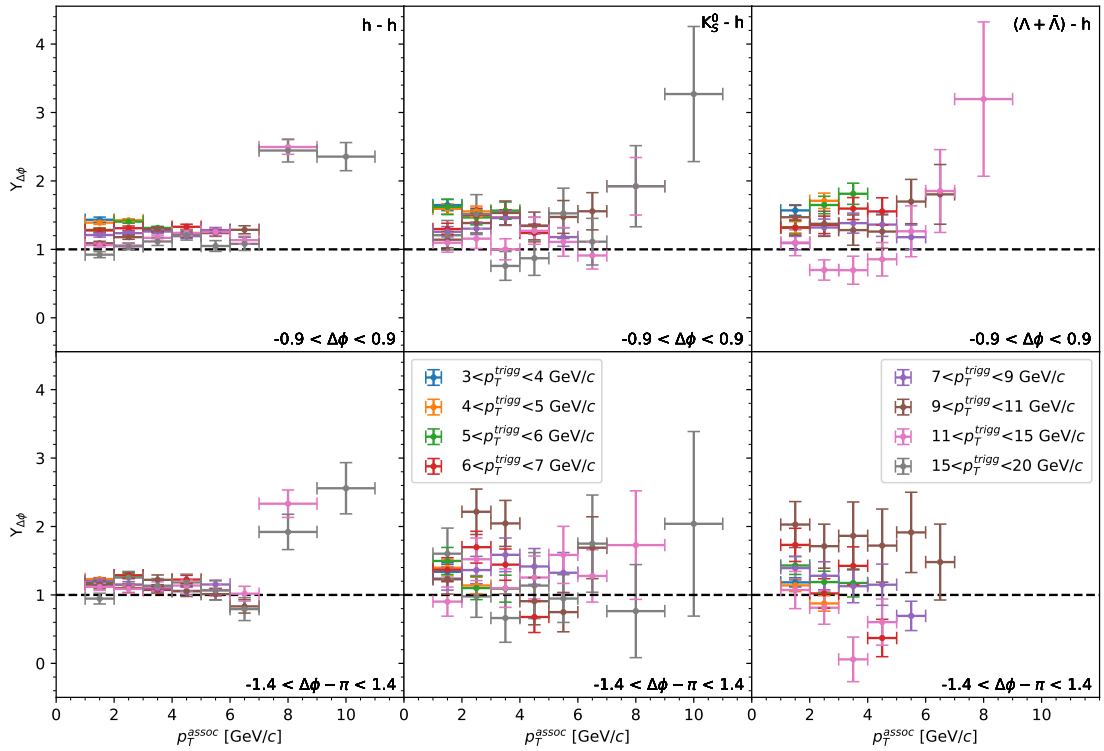

Figure 15: Ratio of PYTHIA to ALICE of per-trigger yields for min. bias as a function of p_T^{assoc}. Near-side peak in the upper row, away-side peak in the lower row for h-h (left), K^0_S-h (middle), $(\Lambda+\overline{\Lambda})$-h (right) correlations.

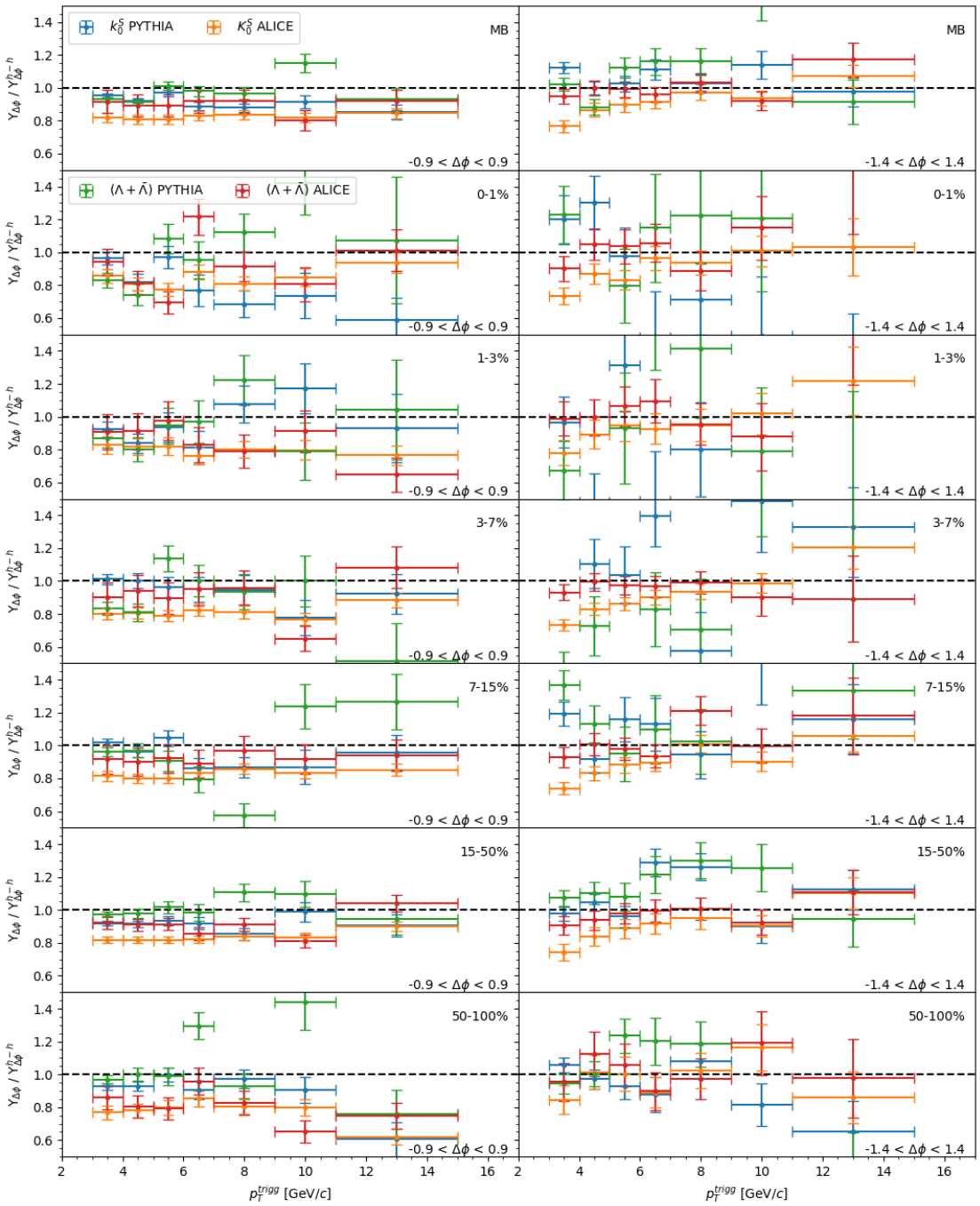

Figure 16: Ratios of K^S_0-h and $(\Lambda+\overline{\Lambda})$-h to h-h per-trigger yields as a function of $p_T^{trigger}$.